JCTC Journal of Chemical Theory and Computation

pubs.acs.org/JCTC Article

Extended Configuration-Interaction Singles Method with Core/Valence Separation (XCIS-CVS): Core-Level Spectra of Open-Shell Molecules

Avik Kumar Ojha and John M. Herbert*

Cite This: J. Chem. Theory Comput. 2025, 21, 12172−12184 Read Online

ACCESS | Metrics & More | Article Recommendations | Supporting Information

ABSTRACT: Spectroscopic core-to-valence transitions serve as reporters on the valence virtual orbitals, which is especially informative for molecules and materials with open-shell ground states that feature (quasi-)degenerate frontier molecular orbitals. Excited states of open-shell molecules are difficult to model using methods based on single excitations only, a category that includes time-dependent density functional theory, due to severe spin contamination (in both ground and excited states) when a spin-unrestricted reference determinant is used. Extended configuration-interaction singles (XCIS) is a simple, variational, and size-consistent wave function *ansatz* that augments the usual CIS excitation space with a limited set of doubly substituted determinants in order to recover spin-pure excited states starting from a restricted open-shell Hartree−Fock (ROHF) ground state. XCIS eliminates spin contamination and offers better accuracy as compared to ROHF-based CIS. Here, we report an implementation of XCIS based on the core/valence separation (CVS) approximation, which restricts the orbital active space to a few occupied orbitals so that core-to-valence transitions can be simulated efficiently. In applications of XCIS-CVS to X-ray transitions in a variety of open-shell systems, including 3d transition metal complexes, we find that both K-edge and pre-edge orbital splittings are reproduced semiquantitatively as compared to experiment.

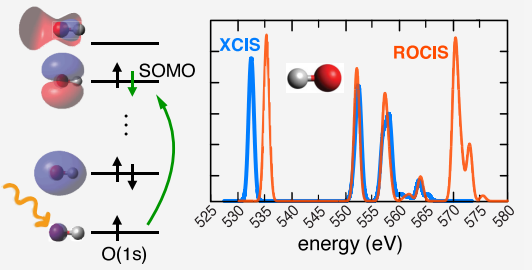

1. INTRODUCTION

X-ray absorption spectroscopy (XAS) is a powerful tool for investigating the local electronic structure and geometrical structure of molecules.[1−7] The localized nature of the initial state (a core orbital) makes XAS an especially sensitive probe of quasi-degenerate frontier energy levels, as are typical in systems with open-shell ground states. Such systems are generally challenging for electronic structure theory.

For closed-shell molecules that are adequately described by a spin-restricted Hartree−Fock (HF) reference state, a simple excitation hierarchy (singles, doubles, ...) provides conceptual clarity and systematic convergence, typically at the level of triple excitations. Time-dependent density-functional theory (TD-DFT) often provides semiquantitative excitation energies,[8,9] while staying within the space of single excitations that limits the cost to $O(N^4)$ with system size, the same as configuration-interaction with single substitutions (CIS).[10] The single-excitation space also provides facile interpretation.[11]

Open-shell ground states bring additional conceptual and computational challenges. Even for systems that do not manifest strong correlation in the usual sense of a small occupied/virtual gap, so that their ground states can be adequately described using a restricted open-shell (RO) reference state,[12−17] CIS excited states still suffer from spin contamination. At the ROCIS level, this leads to significant errors in the low-lying states associated with quasi-degenerate frontier molecular orbitals (MOs).[18] The problem is worse for excited-state calculations based on a spin-unrestricted reference state,[18−21] for which the ground state is spin contaminated as well. Thus, spin contamination is the primary problem for molecules with open-shell ground states, as it affects both large- and small-gap systems, and static correlation is only a secondary consideration in the latter case.

Spin-contamination problems persist in ROCIS calculations (i.e., CIS based on a ROHF reference state),[18] because the singles excitation manifold is not spin-complete and does not afford spin-pure excited states. The problem is especially pronounced for the low-lying excited states that have significant contributions from open-shell orbitals, which are often precisely the states of interest for probing quasi-degenerate frontier MOs. For such systems, ROCIS errors may reach 2−4 eV.[18]

There are a variety of strategies to resolve this in a general way,[22−31] while staying within the basic framework of a single-excitation theory. A particularly appealing choice is the

Received: September 18, 2025
Revised: November 4, 2025
Accepted: November 6, 2025
Published: November 19, 2025

"extended" (X)CIS method,[19] which augments the usual CIS excitation manifold with a limited number of doubly substituted determinants involving the open-shell MOs from a ROHF ground state. The resulting excitation manifold is spin-complete, thereby eliminating spin contamination. This enables XCIS to better characterize the low-lying excited states of open shell systems, as compared to either ROCIS or unrestricted CIS. Because the number of additional determinants does not increase with molecular size, the formal scaling remains the same as that of CIS or TD-DFT, with only a modest prefactor. Like CIS, the XCIS method is variational and size-consistent.[19]

In the present work, we extend the implementation of XCIS in the Q-Chem program[32] to include the core/valence separation (CVS) approximation.[33] For CIS-type wave functions, CVS amounts to restricting the excitation space to a very limited set of active occupied MOs, representing the core orbitals for a given elemental X-ray edge, along with the entire virtual space.[34] This approach is widely used for modeling core-level spectra at the TD-DFT level.[35−41] The XCIS-CVS method reported here retains the aforementioned advantages of conventional XCIS, while extending it to core-level spectroscopy in an efficient way. It provides a robust and low-cost tool for computing core-level spectra of molecules with open-shell ground states, as demonstrated with exemplary calculations presented here.

2. THEORY

2.1. Wave Function *Ansätze*. ROCIS uses a ROHF ground-state reference as the starting point to generate singly substituted determinants. These are shown schematically in Figure 1 for an example with two singly occupied MOs

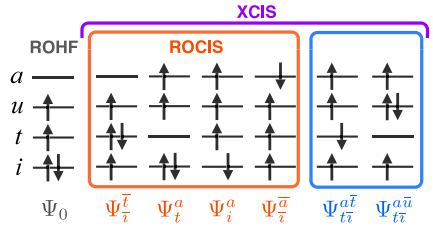

Figure 1. Excitation manifolds for ROCIS and XCIS. At the far left is a high-spin ROHF reference determinant, with two SOMOs ($n_s = 2$) in this particular example. An orange box encloses those singly substituted determinants that are included in a ROCIS calculation. Additional doubly substituted determinants in the blue box are included in XCIS to complete the spin manifold.

(SOMOs). These ground-state MOs are labeled using the following indexing convention: *a*, *b*, *c*, ... for virtual (empty) MOs; *i*, *j*, *k*, ... for doubly occupied MOs; and *t*, *u*, *v*, ... for SOMOs, of which there are $n_s = 2S$ for total spin *S*. The ROCIS *ansatz* is

$$\Psi_{\mathrm{ROCIS}} = \frac{1}{\sqrt{2}} \sum_{ia} c_i^a (\Psi_i^a + \Psi_{\bar{\imath}}^{\bar{a}}) + \sum_{ta} c_t^a \Psi_t^a + \sum_{it} c_{\bar{\imath}}^{\bar{t}} \Psi_{\bar{\imath}}^{\bar{t}} \tag{1}$$

It consists of $i \rightarrow a$ excitations (written as spin-adapted functions $\Psi_i^a + \Psi_{\bar{\imath}}^{\bar{a}}$), $t \rightarrow a$ excitations (Ψ_t^a), and $\bar{\imath} \rightarrow \bar{t}$ excitations ($\Psi_{\bar{\imath}}^{\bar{t}}$).[18] We employ the usual notation for Slater determinants, with a bar (as in $\bar{\imath}$ and $\bar{t}$) to denote β spin. Each individual class of excitations in eq 1 is shown in the ROCIS portion of Figure 1.

The XCIS *ansatz* starts from the same ROHF reference state and includes all of eq 1, along with some doubly substituted determinants as depicted in Figure 1. The latter are spin-adapted to form configuration state functions (CSFs) and allowed to mix with the ROCIS-type single excitations.[19] The resulting wave function is[19,20,27]

$$\Psi_{\mathrm{XCIS}} = \Psi_{\mathrm{ROCIS}} + \sum_{\substack{iatu \\ (t\neq u)}} c_{t\bar{\imath}}^{a\bar{u}} \Psi_{t\bar{\imath}}^{a\bar{u}} + \sum_{ia} \sum_{\lambda=1}^{n_s} \tilde{c}_i^a(\lambda) \tilde{\Psi}_i^a(\lambda) \tag{2}$$

Terms beyond Ψ_{ROCIS} involve selected classes of doubly substituted determinants that are responsible for the most egregious errors in ROCIS calculations.[18] These include $\Psi_{t\bar{\imath}}^{a\bar{u}}$, which requires at least two distinct SOMOs and vanishes for a doublet state with $n_s = 1$. The third term involves determinants labeled $\tilde{\Psi}_i^a(\lambda)$ for $\lambda = 1, ..., n_s$. For $n_s = 1$, the determinants in question are[19]

$$\tilde{\Psi}_i^a(1) = \frac{n_s}{\sqrt{2n_s(n_s+2)}} (\Psi_{\bar{\imath}}^{\bar{a}} - \Psi_i^a) + \frac{2}{\sqrt{2n_s(n_s+2)}} \sum_t \Psi_{t\bar{\imath}}^{a\bar{\imath}} \tag{3}$$

For higher multiplicities, the remaining functions $\tilde{\Psi}_i^a(\lambda)$ are determined by orthogonalizing the determinants $\{\Psi_i^a, \Psi_{\bar{\imath}}^{\bar{a}}, \Psi_{t\bar{\imath}}^{a\bar{\imath}}\}$.[19,27]

Transition energies for either ROCIS or XCIS are computed using a Davidson algorithm,[42] implemented in an integral-direct fashion that involves repeated digestion of electron repulsion integrals with pseudodensities formed from CI coefficients that have been transformed to the atomic orbital (AO) basis.[18−20,43] For XCIS, each doubly substituted determinant has two indices in the SOMO space (see Figure 1), the size of which is limited by shell structure rather than system size. Thus, the number of determinants that are added to the standard ROCIS excitation space is $n_s^2\, n_o n_v$,[20] where n_o and n_v are the number of closed-shell and virtual MOs, respectively. Therefore, the formal cost of XCIS grows as $O(N^4)$ with system size, which is the same scaling as CIS or TD-DFT. (In practice, XCIS is about four times more expensive than CIS for doublets, with a larger prefactor as n_s increases.[19]) This is significantly more efficient than full matrix diagonalization of the CIS Hamiltonian, which scales as $O(N^6)$. The AO-based, integral-direct approach is also much more efficient than MO-based algorithms.

In what follows, we will make comparisons to a similar method implemented in the Orca program,[44] namely, spin-adapted (SA-)ROCIS.[45] This method is called simply "ROCIS" in Orca, yet differs from the original ROCIS *ansatz* in eq 1 by the addition of doubly substituted determinants similar to those used in XCIS. Its wave function corresponds to the following *ansatz*:[45]

$$\Psi_{\mathrm{SA\text{-}ROCIS}} = \Psi_0 + \frac{1}{\sqrt{2}} \sum_{ia} c_i^a (\Psi_i^a + \Psi_{\bar{\imath}}^{\bar{a}}) + \sum_{it} c_{\bar{\imath}}^{\bar{t}} \Psi_{\bar{\imath}}^{\bar{t}} + \sum_{ta} c_t^a \Psi_t^a + \sum_{iat} c_{it}^{ta} \Psi_{it}^{\bar{t}a} + \sum_{\substack{iatu \\ (t\neq u)}} c_{t\bar{\imath}}^{a\bar{u}} \Psi_{t\bar{\imath}}^{a\bar{u}} \tag{4}$$

Inclusion of the reference state Ψ_0 sets SA-ROCIS apart from XCIS, as the former enables a degree of mixing between Ψ_0 and the doubly substituted determinants, which lowers the ground-state energy. The XCIS method deliberately ignores this coupling by excluding Ψ_0 from the *ansatz* in eq 2, in order

https://doi.org/10.1021/acs.jctc.5c01578
J. Chem. Theory Comput. 2025, 21, 12172−12184

to preserve size-consistency.[19] This is a potentially important consideration in a method designed for large molecules.

Another major distinction between SA-ROCIS and XCIS is the construction of spin-adapted CSFs. Whereas XCIS uses a set of orthonormal CSFs $\{\tilde{\Psi}_i^a(\lambda)\}$, SA-ROCIS uses non-orthogonal, spin-adapted CSFs that we indicate by $\bar{\Psi}_{it}^{ta}$ in eq 4. These are defined as[27,45]

$$\bar{\Psi}_{it}^{ta} = \frac{1}{\sqrt{6}}(\Psi_i^a - \Psi_{\bar{t}}^{\bar{a}} - 2\Psi_{t\bar{t}}^{a\bar{t}}) \tag{5}$$

In XCIS, the constants that define $\tilde{\Psi}_i^a(\lambda)$ are different for different values of λ as, for example, in eq 3. These constants depend explicitly on the number of SOMOs (n_s). In eq 5, however, the constant is the same for all spin states. Nevertheless, the sets $\{\bar{\Psi}_{it}^{ta}\}$ and $\{\tilde{\Psi}_i^a(\lambda)\}$ span the same subspace, even though the former are nonorthogonal:[27]

$$S_{tu}^{(i,a)} = \langle \bar{\Psi}_{it}^{ta} | \bar{\Psi}_{iu}^{ua} \rangle \neq \delta_{tu} \tag{6}$$

2.2. CVS Approximation. A conventional implementation of CIS via Davidson's iterative eigensolver makes it prohibitively expensive to reach the core-excited states (except in small molecules with small basis sets),[34] because they lie above numerous valence excited states. However, the significant energy disparity between valence- and core-excited states, combined with the inherent localization of core orbitals, means that matrix elements

$$A_{ia,jb} = \langle \Psi_i^a | \hat{H} | \Psi_j^b \rangle \tag{7}$$

are usually negligible if i is a core orbital and j is a valence orbital. The CVS approximation separates core and valence excitations by neglecting these core/valence couplings.

Operationally, this is achieved by using only a small set of active MOs, corresponding to the core orbitals of interest, along with the full virtual space. Thus, core-to-valence excitations emerge as the lowest-energy states in the spectrum. By varying the nature of the active space in separate calculations, this technique can be used to disentangle contributions from overlapping elemental K-, L-, and M-edges in complex spectra.[34,40,41]

In the present work, we consider only K-edge spectra originating in transitions from 1s orbitals, for which the error introduced by the CVS approximation is negligible.[34,46,47] At an elemental K-edge, this approximation amounts to retaining all of the 1s orbitals for a given element. For example, in order to simulate a carbon K-edge spectrum, one would use an active space consisting of the C(1s) orbital on each carbon atom (along with the full virtual space), with all other occupied MOs treated as inactive. This is illustrated in Figure 2a.

2.3. Intensities. Transition dipole moments

$$\mu_\alpha = \langle \Psi_0 | \hat{\mu}_\alpha | \Psi_n \rangle \tag{8}$$

for $\alpha \in \{x, y, z\}$ are readily evaluated using the Slater−Condon rules, for either ROCIS or XCIS wave functions $|\Psi_n\rangle$. The oscillator strength for this $|0\rangle \rightarrow |n\rangle$ transition is

$$f_{0\rightarrow n} = \frac{2m_e(E_n - E_0)}{3\hbar^2 e^2} \sum_{\alpha=x,y,z} |\mu_\alpha|^2 \tag{9}$$

Absorption spectra are obtained by Gaussian broadening of the vertical transition energies E_n, weighted by oscillator strengths $f_{0\rightarrow n}$.

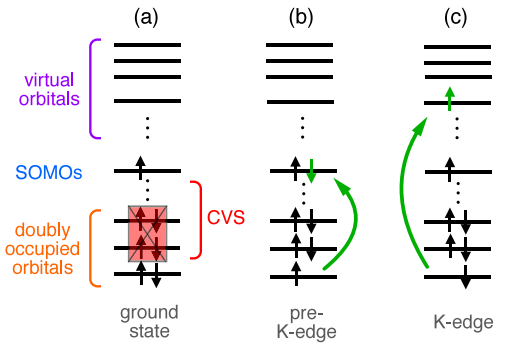

Figure 2. Schematic view of K-edge XAS for an open-shell ground state. (a) All of the occupied MOs are inactive within the CVS approximation except for the elemental core MOs of interest along with any SOMOs. This is illustrated for a doublet state with $n_s = 1$. (b) Excitation from the active core MO into the SOMO results in a pre-edge feature. (c) Excitations into the LUMO and other frontier virtual orbitals, from the elemental 1s orbital, afford the main K-edge and near-edge features.

3. COMPUTATIONAL DETAILS

CVS versions of both ROCIS and XCIS were implemented in a locally modified version of Q-Chem,[32] to be released in v. 6.4. SA-ROCIS calculations[45] were performed using Orca v. 6.0.[44]

3.1. Methods. For most XCIS calculations, we first performed a ground-state calculation using the "different orbitals for different spins" (DODS) version of canonical ROHF,[16] which satisfies both Koopmans and Brillouin conditions and features better handling of non-*Aufbau* solutions to the self-consistent field equations.[15,16] This ROHF variant has better convergence properties, in our experience, and ensures that the MOs have the desired symmetry and spin. The resulting orbitals were then employed as the initial guess for subsequent XCIS calculations. A detailed input file for an XCIS-CVS calculation using Q-Chem is provided in Figure S1. Except where noted, scalar relativistic shifts (taken from ref 48) have been added to calculated excitation energies.

For the small radicals examined in Section 4.1, where comparison is made to benchmark computational results, the aug-cc-pVTZ basis set[49] is used for XCIS, ROCIS, and SA-ROCIS as it provides a balanced description of both core and valence excitations. Note that XAS calculations using CIS and TD-DFT-type methods typically require neither uncontracted core functions nor core−valence polarization functions.[34] For the larger radicals examined in Section 4.2, we used the aug-cc-pVDZ basis set for XCIS.

We will use Karlsruhe basis sets[50,51] for some of the 3d transition metal complexes examined in Section 4.3. (These do not include pseudopotentials, which would be inappropriate for K-edge calculations.) Tests for $[FeCl_4]^-$ indicate that Fe(1s) transition energies computed using XCIS-CVS differ by <2 eV between def2-SVP and def2-TZVP; see Table S1 and Figure S2. Although this is large on the scale of valence transition energies, it is small in comparison to the shifts that are required to match experimental K-edge spectra. This is an important observation given that simulation of an X-ray spectrum may require calculation of hundreds of individual transitions. Diffuse functions matter little for individual transition energies at X-ray edges, although they can affect TD-DFT lineshapes.[40] That said, we do observe significant

https://doi.org/10.1021/acs.jctc.5c01578
J. Chem. Theory Comput. 2025, 21, 12172−12184

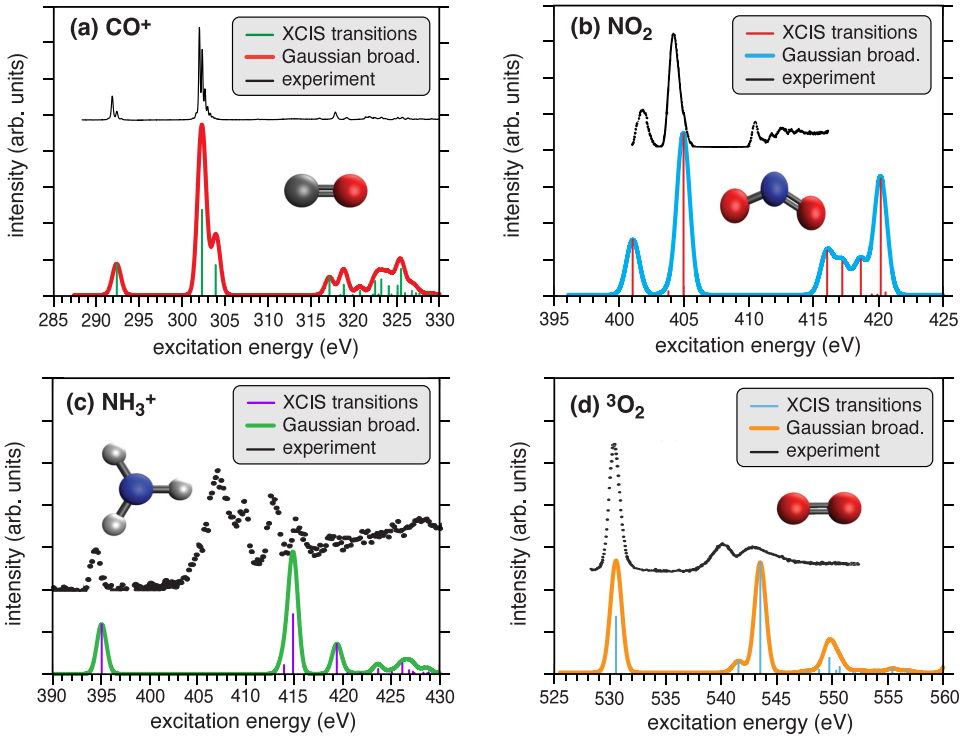

Figure 3. Pre-edge and K-edge XCIS/aug-cc-pVTZ spectra for small radicals, shifted to lower excitation energies to match experiment. Each spectrum contains 10−30 excited states, broadened using a 0.5 eV Gaussian. (a) CO^+ at the carbon K-edge, shifted by 4.79 eV. The experimental spectrum is reproduced with permission from ref 62. CC BY 3.0 license. (b) NO_2 at the nitrogen K-edge, shifted by 8.52 eV. The experimental spectrum is reproduced with permission from ref 67. Copyright 1990 Elsevier. (c) NH_3^+ at the nitrogen K-edge, shifted by 5.71 eV. The experimental spectrum is reproduced with permission from ref 69. CC BY 3.0 license. (d) $^3O_2$ shifted by 11.43 eV. The experimental spectrum is reproduced with permission from ref 73. Copyright 1996 American Physical Society.

differences in absolute excitation energies computed using atomic natural orbital (ANO) basis sets,[52] which will be discussed in Section 4.3.

3.2. Structures. All molecular geometries are provided in the Supporting Information. For small molecules, most geometries were obtained from the Computational Chemistry Comparison and Benchmark Database,[53] which provides reliable experimental and high-level theoretical structures. Some optimized geometries were taken from ref 54. For larger open-shell molecules, we performed geometry optimizations using second-order Møller−Plesset perturbation theory (MP2) with the resolution-of-identity (RI) approximation, using the cc-pVDZ basis set[55] and its corresponding optimized auxiliary basis set for RI.[56] This procedure avoids concern over delocalization errors for DFT geometry optimization of open-shell species.

For the transition metal complexes, geometries were obtained primarily from experimental crystallographic data, or from gas-phase geometry optimizations where crystal structures were unavailable. Specifically, selected Fe and Cu complexes were optimized using the hybrid PBE0 functional,[57] with Grimme's D3 dispersion correction[58] and Becke−Johnson damping.[59] The def2-TZVP basis set[50] was used for these optimizations. Previous work has shown that the PBE0+D3(BJ) functional consistently outperforms semilocal functionals for transition metal geometries.[60]

4. RESULTS AND DISCUSSION

Applications reported here are limited to K-edge XAS, which is an effective method to investigate local electronic structure with elemental specificity. The localized nature of the initial state (a 1s orbital) means that K-edge XAS serves as a reporter on the valence virtual MOs.[1−7] For open shell systems, K-edge XAS involves excitations into either valence SOMOs or unoccupied states (Figure 2b,c), and the resulting spectrum is typically divided into two regions, each offering distinct chemical information.

Pre-edge features manifest as lower-intensity absorption peaks at lower energies as compared to the primary elemental edge, and for an open-shell molecule these may involve excitation into a SOMO. In 3d transition metal complexes, the pre-edge for the K-edge typically corresponds to 1s → 3d transitions, which are dipole-forbidden in centrosymmetric environments due to the $\Delta l = \pm 1$ selection rule, although they are quadrupole-allowed. When inversion symmetry is lifted, however, 3*d*/4p mixing can occur and these pre-edge features may acquire intensity. As such, these features are often quite sensitive to the coordination environment and their transition energies correlate with the metal oxidation state, while the splitting of these 4p-derived features reflects the ligand field and their intensity is related to the covalency of metal−ligand bonding.

4.1. Benchmarks for Small Radicals. Our goal is to assess the accuracy of computational approaches for core-level (K-edge) excitations, so we begin with a benchmark study of small open-shell organic radicals containing second-row elements (carbon, nitrogen, and oxygen). Pre-edge features in these systems arise from the 1s → SOMO transition, which is sensitive to the molecular electronic structure. Small radicals

https://doi.org/10.1021/acs.jctc.5c01578
J. Chem. Theory Comput. 2025, 21, 12172−12184

afford good tests because they possess clearly defined spectral features and experimental reference data are available.[61−74]

Figure 3 depicts pre-edge and main-edge characteristics for the radicals CO^+, NO_2, NH_3^+, and $^3O_2$, comparing XCIS calculations to experiment. The calculations were shifted to lower energy in order to match experiment. These shifts, which range from 4.8−11.4 eV, arise primarily due to incomplete orbital relaxation in single-excitation methods. Nevertheless, the key features of the computed spectra are in good agreement with experimental results.

Table 1 lists the pre-edge excitation energies of small open-shell molecules, including ROCIS, SA-ROCIS, and XCIS

Table 1. Pre-Edge Excitation Energies for Small Radicals[a]

		calculations (eV)[b]				
species	edge	ROCIS	XCIS	SA-ROCIS	expt. (eV)	Δ[c] (eV)
OH	O	535.6	532.5	532.5	525.8[d]	−6.7
CO^+	C	288.9	286.8	286.8	282.0[e]	−4.8
CO^+	O	550.0	546.4	546.4	528.5[e]	−17.9
HO_2	O	537.9	534.9	534.9	528.6[f]	−6.3
CH_3	C	289.6	286.6	286.6	281.4[g]	−5.2
C_2H_5	C	289.9	287.0	287.0	281.7[h]	−5.3
NO	N	409.9	406.7	406.7	399.7[i]	−7.0
NO	O	550.6	546.8	546.8	532.7[i]	−14.1
NO_2	N	412.7	409.5	409.5	401.0[j]	−8.5
NO_2	O	548.0	543.2	543.2	530.3[j]	−12.9
CN	C	286.6	284.3	284.3		
CN	N	412.5	408.8	408.8		
NH_2	N	403.5	400.4	400.4	394.3[k]	−6.1
NH_3^+	N	403.7	400.9	400.9	395.2[l]	−5.7
CH_2Cl	C	290.9	288.0	288.0	282.8[m]	−5.2
CH_2Br	C	290.7	287.8	287.8	282.6[n]	−5.2
allyl	C	292.6	288.0	288.0	282.0[n]	−6.0
*i*Pr radical	C	290.2	287.3	287.3	282.2[h]	−5.1
*t*Bu radical	C	292.1	287.6	287.6	282.6[h]	−5.0
N_2^+	N	405.5	402.1	402.2	394.3[o]	−7.8
$^3O_2$	O	544.9	542.2	539.1	530.8[p]	−11.4
$^3NH_2^+$	N	404.2	402.4	399.9		
MAE[q]		11.0	7.7	7.5		

[a]All species are doublets except for $^3O_2$ and $^3NH_2^+$. [b]aug-cc-pVTZ basis set. See Table S2 for additional decimal places. [c]Deviation between experiment and XCIS. [d]Ref 61. [e]Ref 62. [f]Ref 63. [g]Ref 64. [h]Ref 65. [i]Ref 66. [j]Ref 67. [k]Ref 68. [l]Ref 69. [m]Ref 70. [n]Ref 71. [o]Ref 72. [p]Refs 73 and 74. [q]Mean absolute error (MAE) relative to experiment.

calculations. The ROCIS excitation energies exhibit significant differences as compared to XCIS results. The latter are typically about 3 eV lower than the ROCIS transition energies and in better agreement with experimental values, although shifts (relative to experiment) remain in the range of 5−18 eV.

Species including CO^+, NO_2, and $^3O_2$ exhibit absolute errors around 10 eV using XCIS, or 13 eV for ROCIS. These large differences are mainly due to the lack of orbital relaxation and polarization effects that are especially significant for core-excited species. Core excitation results in a localized hole that strongly polarizes the neighboring electron density, triggering orbital relaxation. In core-ionized states, the relaxation is mainly attractive and stabilizes the system by bringing electron density into the vacant core, whereas the relaxation process is more complicated for a core-excited state where relaxation of the core hole may be partially countered by repulsive polarization among the valence orbitals, due to the promoted electron. This is further complicated in an open-shell system due to electron correlation associated with the SOMOs. Methods such as ROCIS and XCIS do not fully balance these contributions, and large errors may result. Nevertheless, semiquantitative peak splittings can be obtained using XCIS, as in Figure 3.

Orbital relaxation affects not just the transition energies but also the oscillator strengths. In some cases, such as the C(1s) pre-edge of CH_2Cl, we find that both ROCIS and XCIS underestimate intensities for pre-edge transitions (Figure S3). Since absolute errors are large due to incomplete orbital relaxation, it will be important to consider peak splittings since this is the salient experimental observable; theory is not necessary to locate the absolute position of an X-ray edge. Peak splittings are further discussed in Section 4.2.

We next consider the performance of the SA-ROCIS method as implemented in Orca.[45] For all diradicals with doublet ground states, the calculated excitation energies match XCIS values to within 0.01 eV. (Computed excitation energies with additional decimal places can be found in Table S2.) For the triplet ground states, however, major differences are observed in the pre-edge transition energies, including variations of 2.45 eV for $^3NH_2^+$ and 3.10 eV for $^3O_2$.

Figure 4 plots O(1s) spectra of $^3O_2$ obtained from XCIS and SA-ROCIS calculations. The latter spectrum includes 100

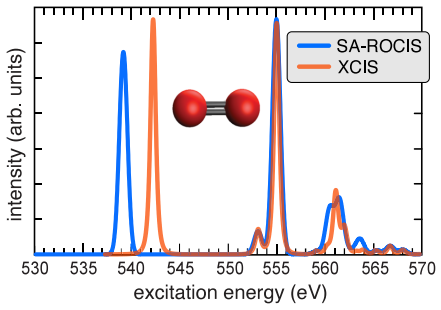

Figure 4. Comparison between K-edge spectra for $^3O_2$ computed using XCIS and SA-ROCIS, with the aug-cc-pVTZ basis set in both cases. The XCIS spectrum includes 45 excited states and the SA-ROCIS spectrum includes 100 excited states. Lorentzian broadening (as implemented in Orca, with a width of 1.0 eV) is used for both spectra.

excited states and terminates at 570 eV but the XCIS spectrum requires only 45 states to reach the same excitation energy. The difference is that the SA-ROCIS calculation affords a significant number of states with zero oscillator strength, between 555 and 570 eV, in the near-edge of the O(1s) spectrum. These states are absent in the XCIS calculation, nevertheless the absorption profile of the main K-edge feature at 555 eV is essentially identical in both spectra. This is followed by a secondary feature centered at 561 eV in both spectra, with similar intensity in either calculation. Additional excited states in the SA-ROCIS calculation may arise from inclusion of the reference determinant Ψ_0 in the SA-ROCIS *ansatz*, which makes little difference when a few low-lying states are computed but apparently lends itself to a larger density of states when ∼ 100 states are included.

A more significant difference between the XCIS and SA-ROCIS spectra for $^3O_2$ is a sizable shift in the pre-edge feature. This may arise in the $\bar{\Psi}_{it}^{ta}$ terms in eq 4 for the SA-ROCIS

https://doi.org/10.1021/acs.jctc.5c01578
J. Chem. Theory Comput. 2025, 21, 12172−12184

ansatz, which are different from the $\tilde{\Psi}_i^a$ terms in the XCIS *ansatz* of eq 2, as discussed in Section 2. These terms involve excitations to the SOMOs (orbital indices t), which are only relevant to pre-edge features. Further support for this explanation is the fact that the constants that define these CSFs, in eqs 3 and 5, are identical for a doublet state with just one SOMO (n_s = 1). For doublet radicals, XCIS and SA-ROCIS spectra agree across the entire energy range.

4.2. Core Excitations for Large Radicals. We next consider several larger molecular species starting with 2,2,6,6-tetramethyl-1-piperidinyloxy ("TEMPO"), for which experimental oxygen and nitrogen K-edge spectra are available.[75] TEMPO is a stable aminoxyl (or nitroxyl, N−O•) radical known for its wide range of applications.[76−80] We have calculated K-edge excitation energies at the XCIS/aug-cc-pVDZ level, for transitions originating from N(1s) or O(1s) orbitals, as shown in Figure 5. As for the smaller radicals,

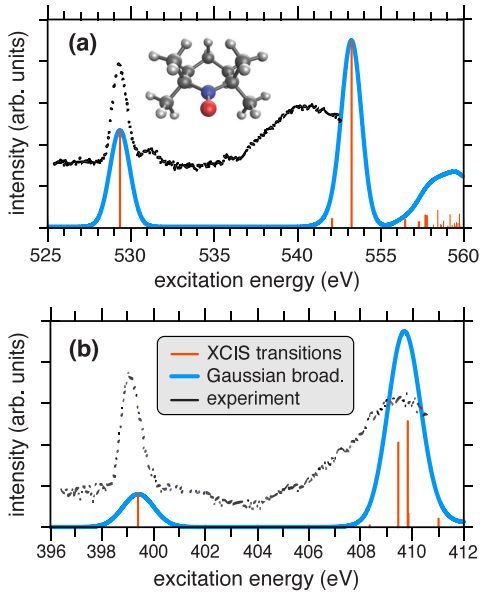

Figure 5. Pre-edge features of the TEMPO radical. XCIS/aug-cc-pVDZ calculations for (a) the O(1s) spectrum and (b) the N(1s) spectrum are shifted to lower energy by 9.68 and 10.41 eV, respectively. These spectra include 10−30 excited states with 0.5 eV Gaussian broadening. Both experimental spectra are reproduced with permission from ref 75. Copyright 2016 The PCCP Owner Societies.

absolute errors in the transition energies are large due to incomplete orbital relaxation, and both XCIS spectra in Figure 5 are shifted to lower energy by about 10 eV in order to match the lowest observed transition.

XCIS usually underestimates peak intensities. Indeed, the N(1s) → SOMO feature in Figure 5b is considerably less intense than the higher-energy N(1s) → LUMO feature, which is not the case in the experimental spectrum although the higher-energy feature is quite broad. A similar but smaller discrepancy is observed in the oxygen K-edge spectra that are shown in Figure 5a. In both cases, the energy gap between the SOMO and LUMO features is underestimated by the XCIS calculations. Although the lack of orbital relaxation may contribute to the error in the splitting, it is likely that the more important contribution to this discrepancy is the ROHF energy levels themselves, and the lack of dynamic correlation in them. In future work, we plan to test this hypothesis with an implementation of XCIS based on a restricted open-shell Kohn−Sham (ROKS) ground state.[81]

We next consider the glutathione radical, which is important in both chemistry and biology,[82,83] and for which a sulfur K-edge spectrum is available from experiment.[84] This is plotted alongside a XCIS/aug-cc-pVDZ calculation in Figure 6. A shift

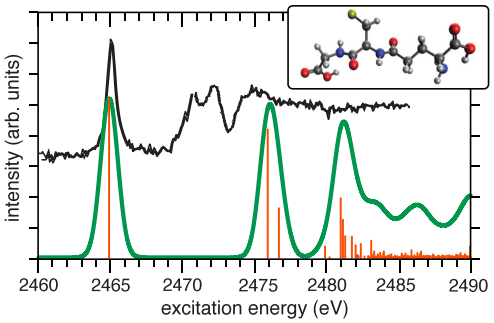

Figure 6. S(1s) spectrum of glutathione radical (inset). The XCIS/aug-cc-pVDZ spectrum includes ca. 300 excited states and is shifted to lower energy by 25.75 eV. (Of this, 6.89 eV can be ascribed to a relativistic shift.[48]) The experimental spectrum is reproduced with permission from ref 84. Copyright 2017 American Chemical Society.

of 26 eV is needed to match experiment, which includes a relativistic correction of 7 eV to the S(1s) energy.[48] The remaining 19 eV is missing orbital relaxation and electron correlation. (Note that the former is a much larger effect than the latter for K-edge transitions.[85]) The XCIS spectrum in Figure 6 shows a large energetic separation between the pre-edge feature, representing the S(1s) → SOMO transition, and the next higher-energy feature, in semiquantitative agreement with experiment.

In Table 2 we compare the XCIS pre-edge transition energies for these two larger radicals to ROCIS results and to

Table 2. K-Edge Excitation Energies for Large Radicals

		excitation energy (eV)			
species	edge	ROCIS[a]	XCIS[a]	expt.	Δ[b] (eV)
TEMPO	O	542.3	539.0	529.3[c]	−9.7
TEMPO	N	413.0	409.8	399.4[d]	−10.4
glutathione	S	2492.7[e]	2491.0[e]	2465.2[f]	−25.8

[a]aug-cc-pVDZ basis set. [b]Deviation between experiment and XCIS. [c]Ref 75. [d]Ref 75. [e]Includes a scalar relativistic shift of 6.89 eV, from ref 48. [f]Ref 84.

experiment. As compared to ROCIS results, XCIS transition energies are closer to experimental values although the differences remain $\gtrsim$ 10 eV. To mitigate these errors, we plan to pursue two strategies in future work. The first is a ROKS-based implementation of XCIS, as mentioned above, which would incorporate some dynamical correlation effects into the one-electron energy levels. An alternative strategy is to use a variant of the static-exchange approximation,[85,86] in which a core-ionized reference state (that might consist of either HF or DFT orbitals) is used to generate MOs that include relaxation of the core hole. For K-edge transitions of closed-shell molecules, errors are reduced to ∼0.5 eV in this way.[85,86]

Finally, we compare XCIS results to a correlated wave function calculation for the phenothiazine cation (PTZ^+), a

https://doi.org/10.1021/acs.jctc.5c01578
J. Chem. Theory Comput. 2025, 21, 12172−12184

relatively stable radical that is an important oxidative species in the chemistry of soft materials.[87−89] The S(1s) spectrum of PTZ^+ has been reported previously at the level of similarity-transformed, equation-of motion coupled-cluster theory (STEOM-CCSD),[90−92] using an unrestricted reference within the CVS approximation.[92] Figure 7 plots this spectrum

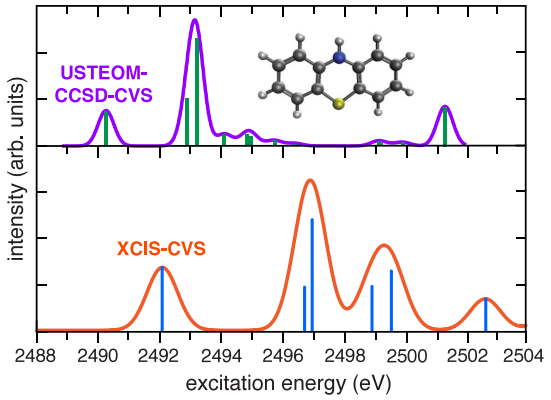

Figure 7. XAS at the sulfur K-edge for PTZ^+ (shown), comparing XCIS and USTEOM-CCSD calculations. Both calculations use the CVS approximation and the cc-pVDZ-DK basis set, and both include 20 excited states. The XCIS calculation includes a relativistic correction of 6.89 eV[48] and Gaussian broadening by 0.5 eV. The USTEOM-CCSD-CVS spectrum includes a Douglas−Kroll−Hess scalar relativistic correction and is reproduced with permission from ref 92. Copyright 2025 American Chemical Society.

alongside the corresponding XCIS-CVS result. Both calculations include a scalar relativistic correction but are otherwise unshifted, so the absolute excitation energies can be compared. The pre-edge feature appears at 2490.4 eV in the USTEOM-CCSD-CVS calculation,[92] versus 2492.1 eV for XCIS-CVS with the same basis set.

The main distinction between these two levels of theory for PTZ^+ is in the separation between the pre-edge and main-edge features, which is larger at the XCIS level. In the XCIS spectrum, two strong peaks emerge in close proximity near 2497 eV, but the corresponding features appear around 2493 eV in the USTEOM-CCSD spectrum. One could explain this discrepancy by how dynamic correlation and orbital relaxations are treated, since the CCSD-based approach includes both, but at the same time there is spin contamination in the USTEOM-CCSD calculation. As such, peak splittings may not adequately represent the quasi-degenerate frontier MOs. Exaggerated peak splittings have also been suggested to be artifacts of HF orbitals in CIS-type calculations.[93]

4.3. Transition Metal Complexes. We next test ROCIS and XCIS for 3d transition metal complexes with open-shell ground states, where strong electron correlation and noticeable relativistic effects make for challenging test cases.

We first consider pre-edge features in the tetrahedral complexes $[FeCl_4]^{2-}$ and $[FeCl_4]^{1-}$, representing ferrous (Fe^{2+}) and ferric (Fe^{3+}) oxidation states, respectively. Compared to centrosymmetric octahedral complexes such as $[FeCl_6]^{3-/2-}$, where the Fe(1s) → Fe(3d) transitions are dipole-forbidden, tetrahedral complexes may exhibit mixing between 3d and 4p orbitals leading to intensity borrowing and pre-edge features in K-edge XAS. Although pre-edge features can still be observed in some octahedral complexes, where they are electric quadrupole-allowed, the pre-edge is dipole-allowed in tetrahedral complexes and typically more intense.

For $[FeCl_4]^{2-}$, a PBE0+D3(BJ)/def2-TZVP geometry optimization affords a slightly distorted tetrahedral geometry with D_{2d} symmetry, consistent with experiment.[94] An XCIS/def2-TZVP calculation at that geometry affords two distinct pre-edge peaks, at 7141.62 and 7142.85 eV, including a relativistic correction of 55.7 eV.[48] These correspond to $^4T_2$ and $^4T_1$ transitions although they differ from the experimental transition energies by 30.02 and 29.73 eV, respectively. The XCIS spectrum of $[FeCl_4]^{2-}$ in Figure 8a has been shifted to

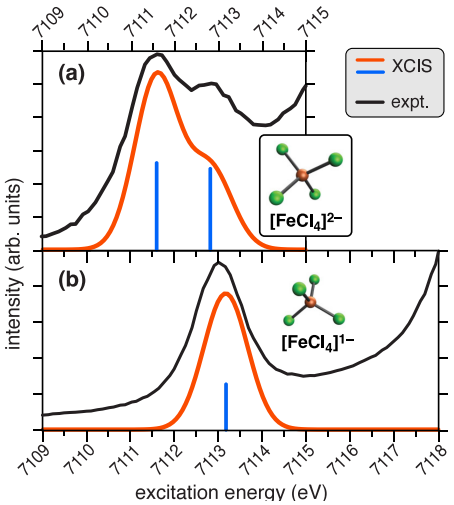

Figure 8. Pre-edge spectra of (a) $[FeCl_4]^{2-}$ and (b) $[FeCl_4]^{1-}$, computed at the XCIS/def2-TZVP level including five excited states in both cases, broadened using a 0.5 eV Gaussian. Computed transition energies are shifted to lower energy by (a) 30.02 and (b) 30.34 eV. Experimental spectra are reproduced with permission from ref 95. Copyright 1997 American Chemical Society.

align it with the experimental spectrum,[95] and the overall spectral envelope is in reasonable agreement with experiment. This includes the $^4T_2/^4T_1$ energy splitting, which is governed by differences in electron repulsion among the 3d orbitals, effectively captured by the relative repulsion between the out-of-plane d_{z^2} orbital and the in-plane $d_{x^2-y^2}$ orbital versus the d_{xy} orbital.[96]

For $[FeCl_4]^-$, we observe a strong $^5T_2$ transition at 7143.54 eV (including the relativistic correction), which deviates from experiment by 30.34 eV. The experimental spectrum is otherwise rather featureless,[95] which is reproduced by the XCIS spectrum (Figure 8b). XCIS spectra for $[FeCl_4]^{2-/1-}$ are clearly accurate enough to distinguish between these two oxidation states.

We next examine oscillator strengths for these two tetrahedral iron complexes. Figure 9 plots the pre-edge spectra for both complexes on the same absolute intensity scale. The corresponding experimental features are shown as well,[95] again comparing intensities for the two oxidation states. The pre-edge intensities are quite different for the two complexes and this is reflected in the XCIS spectra. The origin of the difference is the triply degenerate manifold of t_2 MOs in the Fe^{3+} species, leading to three transitions of nearly equal energy. Upon broadening by 0.5 eV, these transitions merge into a single, intense feature. In contrast, the pre-edge spectrum of the Fe^{2+} species $[FeCl_4]^{2-}$ is relatively diffuse as it involves

https://doi.org/10.1021/acs.jctc.5c01578
J. Chem. Theory Comput. 2025, 21, 12172−12184

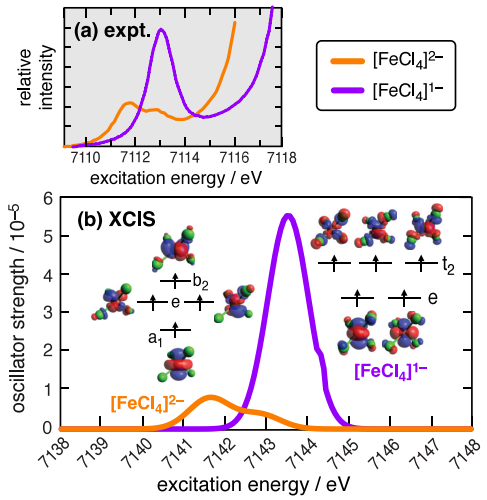

Figure 9. (a) Experimental XAS at the Fe(1s) pre-edge for $[FeCl_4]^{2-}$ and $[FeCl_4]^{1-}$. Reproduced from with permission ref 95. Copyright 1997 American Chemical Society. (b) XCIS/def2-TZVP calculations, including a relativistic shift of 55.7 eV and plotted on an absolute intensity scale, along with frontier MOs for both complexes. In (b), the Cl atoms are shown in green and orbital isosurfaces in red and blue.

transitions among nondegenerate frontier MOs. Proper treatment of degeneracies and splittings among the frontier MOs is required in order to reproduce this effect.

To further benchmark XCIS dipole oscillator strengths, we compare them to results from a multireference restricted active-space (RAS) calculation with a second-order perturbation theory treatment of dynamic correlation (RASPT2).[4,96] Oscillator strengths from that calculation are listed in Table 3

Table 3. Fe(1s) Pre-Edge Excitation Energies and Intensities for $[FeCl_4]^{2-/1-}$

	$(\Delta E)_{XCIS}$ (eV)[a]		osc. str. / 10^{-6}		
			XCIS		
complex (state)	TZVP[b]	ANO[c]	TZVP[b]	ANO[c]	RAS/ANO[d]
$[FeCl_4]^{2-}$ ($^4A_2$)	7140.9	7079.8	0.0	0.0	0.0
$[FeCl_4]^{2-}$ ($^4T_1$)	7141.6	7080.6	4.0	6.5	10.6
$[FeCl_4]^{2-}$ ($^4T_1$)	7142.8	7081.7	3.7	6.1	10.5
$[FeCl_4]^{1-}$ (^5E)	7142.8	7081.8	0.0	0.0	0.0
$[FeCl_4]^{1-}$ ($^5T_2$)	7143.5	7082.6	18.4	27.1	22.7

[a]Including a relativistic shift of 55.7 eV, from ref 48. [b]def2-TZVP basis, where ε = −7114.42 eV for Fe(1s). [c]ANO-RCC-VTZP basis, where ε = −7053.46 eV for Fe(1s). [d]RASPT2/ANO-RCC-VTZP, from ref 96.

for several transitions in $[FeCl_4]^{1-}$ and $[FeCl_4]^{2-}$, alongside XCIS results in two different basis sets: def2-TZVP, which has been used for other 3d transition metal complexes in the present work, and ANO-RCC-VTZP,[97] which was used for the RASPT2 calculations in ref 96.

For all five transitions in $[FeCl_4]^{2-/1-}$ in Table 3, absolute intensities obtained from XCIS calculations are of the same order of magnitude as the RASPT2/ANO-RCC-VTZP results, using either of the aforementioned basis sets for XCIS. At the same time, we observe that XCIS/ANO-RCC-VTZP excitation energies are nearly 50 eV lower than the corresponding def2-TZVP results. This difference is mostly reflected in the Fe(1s) orbital eigenvalues, which are ε = −7114.42 eV (ROHF/def2-TZVP) and ε = −7053.46 eV (ROHF/ANO-RCC-TZVP). It is tempting to conclude that the ANO basis set offers a better description of the Fe(1s) orbital, as it contains Gaussian primitive functions with significantly larger (tighter) exponents, although the magnitude of this effect is surprising. In contrast, an uncontracted version of def2-TZVP affords XCIS excitation energies that are <1 eV different from the XCIS/def2-TZVP values reported in Table 3, consistent with previous basis-set testing.[34]

Moving to a larger 3d metal complex, we consider Cu(II) bis(thiosemicarbazide) sulfate, $Cu(tsc)_2(SO_4)$. This complex exhibits Jahn−Teller distortion at the Cu(II) center,[98] leading to a loss of inversion symmetry that is reflected in our optimized geometry. The PBE0+D3(BJ)/def2-TZVP bond lengths differ from experiment by 0.02−0.05 Å.[99] Due to symmetry breaking, the five-coordinate Cu(II) structure (depicted in Figure 10) features two distinct Cu−N distances and also two Cu−S distances.

XAS at the Cu K-edge is plotted in Figure 10 for this five-coordinate Cu(II) complex, comparing an XCIS/def2-SVPD calculation to an experimental spectrum from ref 100. According to the calculation, the pre-edge arises mainly from a Cu(1s) → Cu($3d^9$) excitation, involving a SOMO with lowered symmetry due to Jahn−Teller distortion. This transition is nominally dipole-forbidden but symmetry-breaking allows an admixture of Cu(4p) character that lends intensity. This important yet subtle feature, which is extremely weak as compared to the Cu K-edge, is adequately modeled at the XCIS level.

4.4. Ligand Effects. Titanium cyclopentadienyl (Cp) compounds including $TiCp_2Cl_2$ and $TiCpCl_3$ have attracted attention for their role in homogeneous catalysis and medicine.[101] Experimentally, XAS at the Ti K-edge reveals that introduction of Cp ligands significantly influences the bonding environment at the Ti center.[102] Notably, while Cp ligands are strong donors, they reduce the degree of 3d/4p mixing between Ti and the chloride ligands, resulting in longer, less covalent Ti−Cl bonds and reduced pre-edge intensity as Cl^- is displaced by Cp^-.[103]

We use a $TiCp_2Cl$ geometry from ref 103 and a $TiCl_3$ geometry that is optimized at the PBE0+D3(BJ)/def2-TZVP level. XCIS Ti(1s) spectra for both species are plotted in Figure 11. The absorption intensity is dramatically smaller for $TiCp_2Cl$ as compared to $TiCl_3$, consistent with the idea that strong ligand donation by Cp^- weakens interactions with spectator ligands and diminishes 3d/4p mixing. The experimental pre-edge feature appears at approximately 4967 eV, while the XCIS calculated peak is located at 4995.53 eV, a difference of 28.5 eV.

These results strongly reinforce the notion that pre-edge features of the metal-K-edge probe both ligand−metal covalency and symmetry breaking in complexes involving 3d transition metal ions. Although XCIS-CVS calculations require large shifts to match experimental K-edge transition energies (which is also true for most TD-DFT methods),[34,104] these results point to the ability of XCIS to accurately simulate subtle changes in electronic structure, providing insight into how particular ligand environments affect core-level excitations in open-shell Ti(III) complexes.

https://doi.org/10.1021/acs.jctc.5c01578
J. Chem. Theory Comput. 2025, 21, 12172−12184

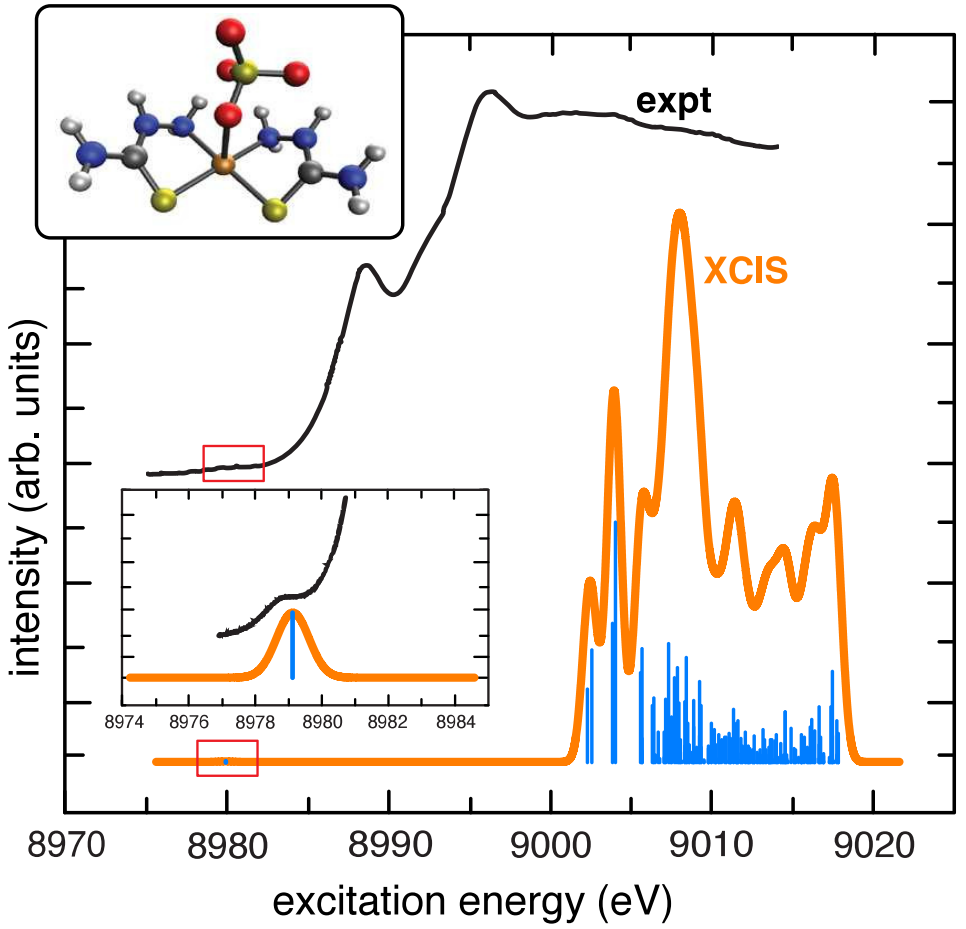

Figure 10. Copper K-edge XAS for $Cu(tsc)_2(SO_4)$. The XCIS/def2-SVPD spectrum was computed from 200 excited states broadened with a 0.5 eV Gaussian and shifted to lower energy by 31.22 eV in order to align the pre-edge feature with experiment (inset). The experimental spectrum is reproduced with permission from ref 100. Copyright 2021 American Chemical Society.

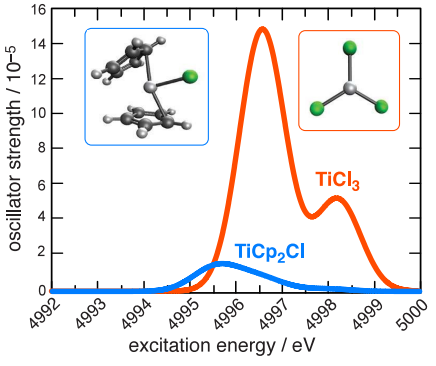

Figure 11. Ti(1s) pre-edge XAS feature in $TiCp_2Cl$ and $TiCl_3$, computed at the XCIS/def2-SVPD level including a relativistic correction of 27.1 eV.[48] Each spectrum is computed from nine excited states, broadened with a 0.5 eV Gaussian.

5. CONCLUSION

We have extended the XCIS method[19] to describe core-to-valence excitations of open-shell molecules, using the CVS approximation. XCIS-CVS retains the $O(N^4)$ computational scaling of CIS and TD-DFT but is rigorously free of spin contamination, in both the ground- and excited-state wave functions. Comparison to experimental K-edge spectra for small, main-group radicals reveals that XCIS-CVS affords a more consistent description of pre-edge features (arising from 1s → SOMO transitions) as compared to the simpler ROCIS-CVS approach that starts from a spin-pure ROHF ground state but admits spin contamination in the excited states. In contrast, XCIS uses a limited set of doubly substituted determinants to achieve proper spin eigenstates. Compared to ROCIS values, XCIS excitation energies tend to be 2−3 eV closer to experiment, although both methods exhibit large absolute errors due to an incomplete treatment of orbital relaxation.

Especially for open-shell molecules, peak splittings are much more important than absolute excitation energies for core-to-valence transitions and the inherent ability of XCIS to resolve quasi-degenerate states offers a clear advantage over ROCIS. This makes XCIS a valuable tool for capturing subtle pre-edge features in X-ray spectra that probe frontier MO energy levels. Comparison between XCIS-CVS and unrestricted (U)-STEOM-CCSD-CVS confirms that the former captures fundamental spectral trends and relative peak spacings reasonably well. We have also demonstrated that XCIS-CVS calculations reproduce spectral signatures in 3d transition metal complexes, including 3d/4p orbital mixing and ligand-field effects. As compared to a spin-adapted version of ROCIS that is implemented in the Orca program,[45] XCIS has the advantage of being size-consistent and thus appropriate for large molecules.

https://doi.org/10.1021/acs.jctc.5c01578
J. Chem. Theory Comput. 2025, 21, 12172−12184

Still, several important features that are necessary for quantitative spectroscopy are missing from the XCIS-CVS method. Chief among these is a treatment of dynamical electron correlation and orbital relaxation, both of which would require a much more expansive set of doubly substituted determinants. In future work, we wish to consider a version of XCIS that is based on a ROKS ground state (i.e., DFT orbitals), rather than the ROHF ground state used in the present work. This would be a low-cost means to incorporate electron correlation that maintains conceptual parallels with XCIS, and has been suggested to reduce the exaggerated spin-multiplet splittings obtained using ROHF orbitals.[93]

Use of DFT orbitals is unlikely to provide much improvement in absolute excitation energies, however, as only a few density functionals outperform CIS for K-edge transition energies.[85] This is related to the fact that the TD-DFT exchange-correlation kernel typically has a negligible effect on core-to-valence excitation energies,[105] and a proper treatment of orbital relaxation is necessary to achieve an absolute accuracy <1 eV in core-level transition energies.[85,86] A route to incorporate orbital relaxation is to combine XCIS with "electron-affinity TD-DFT",[85] which uses reference orbitals from a core-ionized Slater determinant.

Finally, the present applications are limited to K-edge transitions because spin−orbit coupling (SOC) is necessary to describe L-edge transitions.[106] Our group has recently reported CIS and TD-DFT calculations that incorporate SOC, for both L- and M-edge spectra, with pleasing results for closed-shell molecules.[41] In the future, we hope to extend the description of SOC to open-shell molecules using the XCIS *ansatz* to avoid spin contamination.

■ ASSOCIATED CONTENT

Supporting Information

The Supporting Information is available free of charge at https://pubs.acs.org/doi/10.1021/acs.jctc.5c01578.

Additional figures and tables (PDF)

Coordinates for all systems (TXT)

■ AUTHOR INFORMATION

Corresponding Author

John M. Herbert − *Department of Chemistry and Biochemistry, The Ohio State University, Columbus, Ohio 43210, United States;* orcid.org/0000-0002-1663-2278; Email: herbert@chemistry.ohio-state.edu

Author

Avik Kumar Ojha − *Department of Chemistry and Biochemistry, The Ohio State University, Columbus, Ohio 43210, United States;* orcid.org/0009-0005-6283-403X

Complete contact information is available at: https://pubs.acs.org/10.1021/acs.jctc.5c01578

Notes

The authors declare the following competing financial interest(s): J.M.H. is part owner of Q-Chem Inc. and serves on its board of directors.

■ ACKNOWLEDGMENTS

This work was supported by National Science Foundation Grant No. CHE-2402361.

■ REFERENCES

(1) de Groot, F. M. F. XANES spectra of transition metal compounds. *J. Phys. Conf. Ser.* **2009**, *190*, 012004.

(2) Lundberg, M.; Delcey, M. G. Multiconfigurational approach to x-ray spectroscopy of transition metal compounds. In *Transition Metals in Coordination Environments*; Broclawik, E., Borowski, T., Radoń, M., Eds.; Springer Nature: Switzerland, 2019; Vol.*29*, pp 185−217.

(3) Frati, F.; Hunault, M. O. J. Y.; de Groot, F. M. F. Oxygen K-edge x-ray absorption spectra. *Chem. Rev.* **2020**, *120*, 4056−4110.

(4) Bokarev, S. I.; Kühn, O. Theoretical x-ray spectroscopy of transition metal compounds. *Wiley Interdiscip. Rev.: Comput. Mol. Sci.* **2020**, *10*, e1433.

(5) Willey, T. M.; Lee, J. R. I.; Brehmer, D.; Mellone, O. A. P.; Landt, L.; Schreiner, P. R.; Fokin, A. A.; Tkachenko, B. A.; de Meijere, A.; Kozhushkov, S.; van Buuren, A. W. X-ray spectroscopic identification of strain and structure-based resonances in a series of saturated carbon-cage molecules: Adamantane, twistane, octahedrane, and cubane. *J. Vac. Sci. Technol. A* **2021**, *39*, 053208.

(6) Rankine, C. D.; Penfold, T. J. Progress in the theory of x-ray spectroscopy: From quantum chemistry to machine learning and ultrafast dynamics. *J. Phys. Chem. A* **2021**, *125*, 4276−4293.

(7) Vura-Weis, J. Femtosecond extreme ultraviolet absorption spectroscopy of transition metal complexes. *Annu. Rev. Phys. Chem.* **2025**, *76*, 455−470.

(8) Laurent, A. D.; Jacquemin, D. TD-DFT benchmarks: A review. *Int. J. Quantum Chem.* **2013**, *113*, 2019−2039.

(9) Herbert, J. M. Density-functional theory for electronic excited states. In *Theoretical and Computational Photochemistry: Fundamentals, Methods, Applications and Synergy with Experimental Approaches*; García-Iriepa, C., Marazzi, M., Eds.; Elsevier: Amsterdam, 2023; Chapter 3, pp 69−118.

(10) Foresman, J. B.; Head-Gordon, M.; Pople, J. A.; Frisch, M. J. Toward a systematic molecular orbital theory for excited states. *J. Phys. Chem.* **1992**, *96*, 135−149.

(11) Herbert, J. M. Visualizing and characterizing excited states from time-dependent density functional theory. *Phys. Chem. Chem. Phys.* **2024**, *26*, 3755−3794.

(12) Roothaan, C. C. J. Self-consistent field theory for open shells of electronic systems. *Rev. Mod. Phys.* **1960**, *32*, 179−185.

(13) Filatov, M.; Shaik, S. Spin-restricted density functional approach to the open-shell problem. *Chem. Phys. Lett.* **1998**, *288*, 689−697.

(14) Tsuchimochi, T.; Scuseria, G. E. Communication: ROHF theory made simple. *J. Chem. Phys.* **2010**, *133*, 141102.

(15) Plakhutin, B. N.; Davidson, E. R. Koopmans' theorem in the restricted open-shell Hartree-Fock method. 1. A variational approach. *J. Phys. Chem. A* **2009**, *113*, 12386−12395.

(16) Plakhutin, B. N.; Davidson, E. R. Canonical form of the Hartree-Fock orbitals in open-shell systems. *J. Chem. Phys.* **2014**, *140*, 014102.

(17) Plakhutin, B. N.; Novikov, A. V.; Polygalova, N. E.; Prokhorov, T. E. On the ordering of orbital energies in the ROHF method: Koopmans' theorem versus Aufbau principle. In *Quantum Systems in Physics, Chemistry, and Biology*; Tadjer, A., Pavlov, R., Maruani, J., Brändas, E. J., Delgado-Barrio, G., Eds.; Springer International Publishing: Cham, Switzerland, 2017; Vol.*30*, pp 17−38.

(18) Maurice, D.; Head-Gordon, M. Configuration interaction with single substitutions for excited states of open-shell molecules. *Int. J. Quantum Chem. Symp.* **1995**, *56*, 361−370.

(19) Maurice, D.; Head-Gordon, M. On the nature of electronic transitions in radicals: An extended single excitation configuration interaction method. *J. Phys. Chem.* **1996**, *100*, 6131−6137.

(20) Maurice, D. R. Single Electron Theories of Excited States. *Ph.D. Thesis*, University of California, 1998.

(21) Ipatov, A.; Cordova, F.; Doriol, L. J.; Casida, M. E. Excited-state spin-contamination in time-dependent density-functional theory for molecules with open-shell ground states. *J. Mol. Struct. (Theochem)* **2009**, *914*, 60−73.

(22) Sears, J. S.; Sherrill, C. D.; Krylov, A. I. A spin-complete version of the spin-flip approach to bond breaking: What is the impact of obtaining spin eigenfunctions? *J. Chem. Phys.* **2003**, *118*, 9084−9094.
(23) Vahtras, O.; Rinkevicius, Z. General excitations in time-dependent density functional theory. *J. Chem. Phys.* **2007**, *126*, 114101.
(24) Li, Z.; Liu, W. Spin-adapted open-shell random phase approximation and time-dependent density functional theory. I. Theory. *J. Chem. Phys.* **2010**, *133*, 064106.
(25) Li, Z.; Liu, W.; Zhang, Y.; Suo, B. Spin-adapted open-shell time-dependent density functional theory. II. Theory and pilot application. *J. Chem. Phys.* **2011**, *134*, 134101.
(26) Li, Z.; Liu, W. Spin-adapted open-shell time-dependent density functional theory. III. An even better and simpler formulation. *J. Chem. Phys.* **2011**, *135*, 194106.
(27) Wang, Z.; Li, Z.; Zhang, Y.; Liu, W. Analytic energy gradients of spin-adapted open-shell time-dependent density functional theory. *J. Chem. Phys.* **2020**, *153*, 164109.
(28) Zhang, X.; Herbert, J. M. Spin-flip, tensor equation-of-motion configuration interaction with a density-functional correction: A spin-complete method for exploring excited-state potential energy surfaces. *J. Chem. Phys.* **2015**, *143*, 234107.
(29) Herbert, J. M., Mandal, A. Spin-flip TDDFT for photochemistry. In *Time-Dependent Density-Functional Theory: Nonadiabatic Molecular Dynamics*; Zhu, C., Ed.; Jenny Stanford: Singapore, 2023; Chapter 10, pp 361−404.
(30) Mato, J.; Gordon, M. S. A general spin-complete spin-flip configuration interaction method. *Phys. Chem. Chem. Phys.* **2018**, *20*, 2615−2626.
(31) Mato, J.; Gordon, M. S. Analytic gradients for the spin-flip ORMAS-CI method: Optimizing minima, saddle points, and conical intersections. *J. Phys. Chem. A* **2019**, *123*, 1260−1272.
(32) Epifanovsky, E.; et al. Software for the frontiers of quantum chemistry: An overview of developments in the Q-Chem 5 package. *J. Chem. Phys.* **2021**, *155*, 084801.
(33) Norman, P.; Dreuw, A. Simulating x-ray spectroscopies and calculating core-excited states of molecules. *Chem. Rev.* **2018**, *118*, 7208−7248.
(34) Herbert, J. M.; Zhu, Y.; Alam, B.; Ojha, A. K. Time-dependent density functional theory for x-ray absorption spectra: Comparing the real-time approach to linear response. *J. Chem. Theory Comput.* **2023**, *19*, 6745−6760.
(35) Besley, N. A. Modeling of the spectroscopy of core electrons with density functional theory. *Wiley Interdiscip. Rev.: Comput. Mol. Sci.* **2021**, *11*, e1527.
(36) Bussy, A.; Hutter, J. Efficient and low-scaling linear-response time-dependent density functional theory implementation for core-level spectroscopy of large and periodic systems. *Phys. Chem. Chem. Phys.* **2021**, *23*, 4736−4746.
(37) Bussy, A.; Hutter, J. First-principles correction scheme for linear-response time-dependent density functional theory calculations of core electronic states. *J. Chem. Phys.* **2021**, *155*, 034108.
(38) Fransson, T.; Pettersson, L. G. M. Evaluating the impact of the Tamm-Dancoff approximation on x-ray spectrum calculations. *J. Chem. Theory Comput.* **2024**, *20*, 2181−2191.
(39) Fransson, T.; Pettersson, L. G. M. TDDFT and the x-ray absorption spectrum of liquid water: Finding the "best" functional. *J. Chem. Phys.* **2024**, *160*, 234105.
(40) Mandal, A.; Berquist, E. J.; Herbert, J. M. A new parameterization of the DFT/CIS method with applications to core-level spectroscopy. *J. Chem. Phys.* **2024**, *161*, 044114.
(41) Mandal, A.; Herbert, J. M. Computing L- and M-edge spectra using the DFT/CIS method with spin-orbit coupling. *Phys. Chem. Chem. Phys.* **2025**, *27*, 16336−16353.
(42) Leininger, M. L.; Sherrill, C. D.; Allen, W. D.; Schaefer, H. F., III Systematic study of selected diagonalization methods for configuration interaction matrices. *J. Comput. Chem.* **2001**, *22*, 1574−1589.
(43) Morrison, A. F.; Epifanovsky, E.; Herbert, J. M. Double-buffered, heterogeneous CPU + GPU integral digestion algorithm for single-excitation calculations involving a large number of excited states. *J. Comput. Chem.* **2018**, *39*, 2173−2182.
(44) Neese, F. Software update: The ORCA program system−version 6.0. *Wiley Interdiscip. Rev.: Comput. Mol. Sci.* **2025**, *15*, e70019.
(45) Roemelt, M.; Neese, F. Excited states of large open-shell molecules: An efficient, general, and spin-adapted approach based on a restricted open-shell ground state wave function. *J. Phys. Chem. A* **2013**, *117*, 3069−3083.
(46) Herbst, M. F.; Fransson, T. Quantifying the error of the core-valence separation approximation. *J. Chem. Phys.* **2020**, *153*, 054114.
(47) Helmich-Paris, B. Simulating X-ray absorption spectra with complete active space self-consistent field linear response methods. *Int. J. Quantum Chem.* **2021**, *121*, e26559.
(48) Takahashi, O. Relativistic corrections for single- and double-core excitations at the K- and L-edges from Li to Kr. *Comput. Theor. Chem.* **2017**, *1102*, 80−86.
(49) Kendall, R. A.; Dunning, T. H., Jr.; Harrison, R. J. Electron affinities of the first-row atoms revisited. Systematic basis sets and wave functions. *J. Chem. Phys.* **1992**, *96*, 6796−6806.
(50) Weigend, F.; Ahlrichs, R. Balanced basis sets of split valence, triple zeta valence and quadruple zeta valence quality for H to Rn: Design and assessment of accuracy. *Phys. Chem. Chem. Phys.* **2005**, *7*, 3297−3305.
(51) Rappoport, D.; Furche, F. Property-optimized Gaussian basis sets for molecular response calculations. *J. Chem. Phys.* **2010**, *133*, 134105.
(52) Almlöf, J.; Taylor, P. R. Atomic natural orbital (ANO) basis sets for quantum chemical calculations. *Adv. Quantum Chem.* **1991**, *22*, 301−373.
(53) Johnson, R. D. Computational Chemistry Comparison and Benchmark Database. http://cccbdb.nist.gov (accessed 2025−09−03).
(54) Hait, D.; Haugen, E. A.; Yang, Z.; Oosterbaan, K. J.; Leone, S. R.; Head-Gordon, M. Accurate prediction of core-level spectra of radicals at density functional theory cost via square gradient minimization and recoupling of mixed configurations. *J. Chem. Phys.* **2020**, *153*, 134108.
(55) Dunning, T. H., Jr. Gaussian basis sets for use in correlated molecular calculations. I. The atoms boron through neon and hydrogen. *J. Chem. Phys.* **1989**, *90*, 1007−1023.
(56) Weigend, F.; Häser, M.; Patzelt, H.; Ahlrichs, R. RI-MP2: Optimized auxiliary basis sets and demonstration of efficiency. *Chem. Phys. Lett.* **1998**, *294*, 143−152.
(57) Adamo, C.; Barone, V. Toward reliable density functional methods without adjustable parameters: The PBE0 model. *J. Chem. Phys.* **1999**, *110*, 6158−6170.
(58) Grimme, S.; Antony, J.; Ehrlich, S.; Krieg, H. A consistent and accurate ab initio parameterization of density functional dispersion correction (DFT-D) for the 94 elements H-Pu. *J. Chem. Phys.* **2010**, *132*, 154104.
(59) Grimme, S.; Ehrlich, S.; Goerigk, L. Effect of the damping function in dispersion corrected density functional theory. *J. Comput. Chem.* **2011**, *32*, 1456−1465.
(60) Bühl, M.; Reimann, C.; Pantazis, D. A.; Bredow, T.; Neese, F. Geometries of third-row transition-metal complexes from density-functional theory. *J. Chem. Theory Comput.* **2008**, *4*, 1449−1459.
(61) Stranges, S.; Richter, R.; Alagia, M. High-resolution inner-shell photoabsorption of the OH and OD free radicals. *J. Chem. Phys.* **2002**, *116*, 3676−3680.
(62) Couto, R. C.; Kjellsson, L.; Ågren, H.; Carravetta, V.; Sorensen, S. L.; Kubin, M.; Bülow, C.; Timm, M.; Zamudio-Bayer, V.; von Issendorff, B.; Lau, J. T.; Söderström, J.; Rubensson, J.-E.; Lindblad, R. The carbon and oxygen K-edge NEXAFS spectra of CO^+. *Phys. Chem. Chem. Phys.* **2020**, *22*, 16215−16223.
(63) Lacombe, S.; Bournel, F.; Laffon, C.; Parent, P. Radical photochemistry in oxygen-loaded ices. *Angew. Chem., Int. Ed. Engl.* **2006**, *45*, 4159−4163.

(64) Alagia, M.; Lavollée, M.; Richter, R.; Ekström, U.; Carravetta, V.; Stranges, D.; Brunetti, B.; Stranges, S. Probing the potential energy surface by high-resolution x-ray absorption spectroscopy: The umbrella motion of the core-excited CH_3 free radical. *Phys. Rev. A* **2007**, *76*, 022509.
(65) Yang, Z. Characterization of Substituted Radicals by Multi-Edge Femtosecond X-Ray Transient Absorption Spectroscopy. *Ph.D. Thesis*, University of California, Berkeley, 2018.
(66) Wight, G. R.; Brion, C. E. K-shell excitations in NO and O_2 by 2.5 keV electron impact. *J. Electron Spectrosc.* **1974**, *4*, 313−325.
(67) Zhang, W.; Sze, K. H.; Brion, C. E.; Tong, X. M.; Li, J. M. Inner-shell electron loss spectra of NO_2 at high resolution: Comparison with multichannel quantum defect calculations of dipole oscillator strengths and transition energies. *Chem. Phys.* **1990**, *140*, 265−279.
(68) Parent, P.; Bournel, F.; Lasne, J.; Lacombe, S.; Strazzulla, G.; Gardonio, S.; Lizzit, S.; Kappler, J.-P.; Joly, L.; Laffon, C.; Carniato, S. The irradiation of ammonia ice studied by near edge x-ray absorption spectroscopy. *J. Chem. Phys.* **2009**, *131*, No. 154308.
(69) Bari, S.; Inhester, L.; Schubert, K.; Mertens, K.; Schunck, J. O.; Dörner, S.; Deinert, S.; Schwob, L.; Schippers, S.; Müller, A.; Klumpp, S.; Martins, M. Inner-shell x-ray absorption spectra of the cationic series NH_y^+ (y = 0−3). *Phys. Chem. Chem. Phys.* **2019**, *21*, 16505−16514.
(70) Yang, Z.; Schnorr, K.; Bhattacherjee, A.; Lefebvre, P.-L.; Epshtein, M.; Xue, T.; Stanton, J. F.; Leone, S. R. Electron-withdrawing effects in the photodissociation of CH_2ICl to form CH_2Cl radical, simultaneously viewed through the carbon K and chlorine $L_{2,3}$ x-ray edge. *J. Am. Chem. Soc.* **2018**, *140*, 13360−13366.
(71) Alagia, M.; Bodo, E.; Decleva, P.; Falcinelli, S.; Ponzi, A.; Richter, R.; Stranges, S. The soft x-ray absorption spectrum of the allyl free radical. *Phys. Chem. Chem. Phys.* **2013**, *15*, 1310−1318.
(72) Lindblad, R.; Kjellsson, L.; Couto, R. C.; Timm, M.; Bülow, C.; Zamudio-Bayer, V.; Lundberg, M.; von Issendorff, B.; Lau, J. T.; Sorensen, S. L.; Carravetta, V.; Ågren, H.; Rubensson, J.-E. X-ray absorption spectrum of the N_2^+ molecular ion. *Phys. Rev. Lett.* **2020**, *124*, 203001.
(73) Glans, P.; Gunnelin, K.; Skytt, P.; Guo, J.-H.; Wassdahl, N.; Nordgren, J.; Ågren, H.; Gel'mukhanov, F. K.; Warwick, T.; Rotenberg, E. Resonant x-ray emission spectroscopy of molecular oxygen. *Phys. Rev. Lett.* **1996**, *76*, 2448−2451.
(74) Coreno, M.; de Simone, M.; Prince, K. C.; Richter, R.; Vondráček, M.; Avaldi, L.; Camilloni, R. Vibrationally resolved oxygen K →Π* spectra of O_2 and CO. *Chem. Phys. Lett.* **1999**, *306*, 269−274.
(75) Ljubić, I.; Kivimäki, A.; Coreno, M. An experimental NEXAFS and computational TDDFT and ΔDFT study of the gas-phase core excitation spectra of nitroxide free radical TEMPO and its analogues. *Phys. Chem. Chem. Phys.* **2016**, *18*, 10207−10217.
(76) Shinoda, R.; Saito, T.; Okita, Y.; Isogai, A. Relationship between length and degree of polymerization of TEMPO-oxidized cellulose nanofibrils. *Biomacromolecules* **2012**, *13*, 842−849.
(77) Kim, J.-K.; Matic, A.; Ahn, J.-H.; Jacobsson, P.; Song, C.-E. Preparation and application of TEMPO-based di-radical organic electrode with ionic liquid-based polymer electrolyte. *RSC Adv.* **2012**, *2*, 10394−10399.
(78) Rahimi, A.; Azarpira, A.; Kim, H.; Ralph, J.; Stahl, S. Chemoselective metal-free aerobic alcohol oxidation in lignin. *J. Am. Chem. Soc.* **2013**, *135*, 6415−6418.
(79) Halbmair, K.; Seikowski, J.; Tkach, I.; Höbartner, C.; Sezer, D.; Bennati, M. High-resolution measurement of long-range distances in RNA: Pulse EPR spectroscopy with TEMPO-labeled nucleotides. *Chem. Sci.* **2016**, *7*, 3172−3180.
(80) Spier, V. C.; Sierakowski, M. R.; Reed, W. F.; de Freitas, R. A. Polysaccharide depolymerization from TEMPO-catalysis: Effect of TEMPO concentration. *Carbohydr. Polym.* **2017**, *170*, 140−147.
(81) Okazaki, I.; Sato, F.; Yoshihiro, T.; Ueno, T.; Kashiwagi, H. Development of a restricted open shell Kohn-Sham program and its application to a model heme complex. *J. Mol. Struct. (Theochem)* **1998**, *451*, 109−119.
(82) Ma, Q.; Wang, M.; Cai, H.; Li, F.; Fu, S.; Liu, Y.; Zhao, Y. A sensitive and rapid detection of glutathione based on a fluorescence-enhanced "turn-on" strategy. *J. Mater. Chem. B* **2021**, *9*, 3563−3572.
(83) Hossain, M. K.; Huang, G. G.; Hossain, M. M. Novel methods for the detection of glutathione by surface-enhanced Raman scattering: A perspective review. *Heliyon* **2025**, *11*, e41588.
(84) Sneeden, E. Y.; Hackett, M. J.; Cotelesage, J. J. H.; Prince, R. C.; Barney, M.; Goto, K.; Block, E.; Pickering, I. J.; George, G. N. Photochemically generated thiyl free radicals observed by x-ray absorption spectroscopy. *J. Am. Chem. Soc.* **2017**, *139*, 11519−11526.
(85) Carter-Fenk, K.; Cunha, L. A.; Arias-Martinez, J. E.; Head-Gordon, M. Electron-affinity time-dependent density functional theory: Formalism and applications to core-excited states. *J. Phys. Chem. Lett.* **2022**, *13*, 9664−9672.
(86) Hait, D.; Oosterbaan, K. J.; Carter-Fenk, K.; Head-Gordon, M. Computing x-ray absorption spectra from linear-response particles atop optimized holes. *J. Chem. Phys.* **2022**, *156*, 201104.
(87) Christensen, J. A.; Phelan, B. T.; Chaudhuri, S.; Acharya, A.; Batista, V. S.; Wasielewski, M. R. Phenothiazine radical cation excited states as super-oxidants for energy-demanding ractions. *J. Am. Chem. Soc.* **2018**, *140*, 5290−5299.
(88) Noda, L. K.; Gonçalves, N. S. Assignment of the electronic transition of phenothiazine radical cation in the visible region−a resonance Raman spectroscopy and theoretical investigation. *J. Mol. Struct.* **2019**, *1191*, 253−258.
(89) Zhou, J.; Mao, L.; Wu, M.-X.; Peng, Z.; Yang, Y.; Zhou, M.; Zhao, X.-L.; Shi, X.; Yang, H.-B. Extended phenothiazines: Synthesis, photophysical and redox properties, and efficient photocatalytic oxidative coupling of amines. *Chem. Sci.* **2022**, *13*, 5252−5260.
(90) Nooijen, M.; Bartlett, R. J. A new method for excited states: Similarity transformed equation-of-motion coupled-cluster theory. *J. Chem. Phys.* **1997**, *106*, 6441−6448.
(91) Casanova-Páez, M.; Neese, F. Assessment of the simalarity-transformed equation of motion (STEOM) for open-shell organic and transition metal molecules. *J. Chem. Phys.* **2024**, *161*, 144120.
(92) Casanova-Páez, M.; Neese, F. Core-excited states for open-shell systems in similarity-transformed equation-of-motion theory. *J. Chem. Theory Comput.* **2025**, *21*, 1306−1321.
(93) Roemelt, M.; Maganas, D.; DeBeer, S.; Neese, F. A combined DFT and restricted open-shell configuration interaction method including spin-orbit coupling: Application to transition metal L-edge x-ray absorption spectroscopy. *J. Chem. Phys.* **2013**, *138*, 204101.
(94) Lauher, J. W.; Ibers, J. A. Structure of tetramethylammonium tetrachloroferrate(II). Comparison of iron(II) and iron(III) bond lengths in high-spin tetrahedral environments. *Inorg. Chem.* **1975**, *14*, 348−352.
(95) Westre, T. E.; Kennepohl, P.; DeWitt, J. G.; Hedman, B.; Hodgson, K. O.; Solomon, E. I. A multiplet analysis of Fe K-edge 1s → 3d pre-edge features of iron complexes. *J. Am. Chem. Soc.* **1997**, *119*, 6297−6314.
(96) Guo, M.; Sørensen, L. K.; Delcey, M. G.; Pinjari, R. V.; Lundberg, M. Simulations of iron K pre-edge X-ray absorption spectra using the restricted active space method. *Phys. Chem. Chem. Phys.* **2016**, *18*, 3250−3259.
(97) Roos, B. O.; Lindh, R.; Malmqvist, P.-Å; Veryazov, V.; Widmark, P.-O. New relativistic ANO basis sets for transition metal atoms. *J. Phys. Chem. A* **2005**, *109*, 6575−6579.
(98) Orgel, L. E. 929. The effects of crystal fields on the properties of transition-metal ions. *J. Chem. Soc.* **1952**, 4756−4761.
(99) Villa, A. C.; Manfredotti, A. G.; Guastini, C. Bis-(thio-semi-carbazide) copper(II) sulfate, $C_2H_{10}CuN_8O_6S_2$. *Cryst. Struct. Commun.* **1972**, *1*, 125−128.
(100) Frank, P.; Benfatto, M. Symmetry breaking in solution-phase $[Cu(tsc)_2(H_2O)_2]^{2+}$: Emergent asymmetry in Cu−S distances and in covalence. *J. Phys. Chem. B* **2021**, *125*, 10779−10796.
(101) Cini, M.; Bradshaw, T. D.; Woodward, S. Using titanium complexes to defeat cancer: The view from the shoulders of titans. *Chem. Soc. Rev.* **2017**, *46*, 1040−1051.

https://doi.org/10.1021/acs.jctc.5c01578
J. Chem. Theory Comput. 2025, 21, 12172−12184

(102) DeBeer George, S.; Brant, P.; Solomon, E. I. Metal and ligand K-edge XAS of organotitanium complexes: Metal 4p and 3d contributions to pre-edge intensity and their contributions to bonding. *J. Am. Chem. Soc.* **2005**, *127*, 667−674.
(103) DeBeer George, S.; Huang, K.-W.; Waymouth, R. M.; Solomon, E. L. Metal and ligand K-edge XAS of titanium-TEMPO complexes: Determination of oxidation states and insights into Ti−O bond homolysis. *Inorg. Chem.* **2006**, *45*, 4468−4477.
(104) Fransson, T.; Brumboiu, I. E.; Vidal, M. L.; Norman, P.; Coriani, S.; Dreuw, A. XABOOM: An x-ray absorption benchmark of organic molecules based on carbon, nitrogen, and oxygen 1s $\rightarrow\pi^*$ transitions. *J. Chem. Theory Comput.* **2021**, *17*, 1618−1637.
(105) Pak, S.; Nascimento, D. R. The role of the coupling matrix elements in time-dependent density functional theory on the simulation of core-level spectra of transition metal complexes. *Electron. Struct.* **2024**, *6*, 015014.
(106) Kasper, J. M.; Stetina, T. F.; Jenkins, A. J.; Li, X. Ab initio methods for L-edge x-ray absorption spectroscopy. *Chem. Phys. Rev.* **2020**, *1*, 011304.

https://doi.org/10.1021/acs.jctc.5c01578
J. Chem. Theory Comput. 2025, 21, 12172−12184